



RESEARCH LETTER

10.1002/2015GL066581

Key Points:

- EMIC waves are thought to be highly important drivers of electron loss from the outer radiation belt
- To date, there are few experimental examples of precipitation-causing EMIC events
- Simultaneous in situ EMIC wave, plasma, and precipitation flux measurements made for the first time

Correspondence to:

C. J. Rodger,
crodrger@physics.otago.ac.nz

Citation:

Rodger, C. J., A. T. Hendry, M. A. Clilverd, C. A. Kletzing, J. B. Brundell, and G. D. Reeves (2015), High-resolution in situ observations of electron precipitation-causing EMIC waves, *Geophys. Res. Lett.*, 42, 9633–9641, doi:10.1002/2015GL066581.

Received 13 OCT 2015

Accepted 17 OCT 2015

Accepted article online 21 OCT 2015

Published online 21 NOV 2015

High-resolution in situ observations of electron precipitation-causing EMIC waves

Craig J. Rodger¹, Aaron T. Hendry¹, Mark A. Clilverd², Craig A. Kletzing³, James B. Brundell¹, and Geoffrey D. Reeves⁴
¹Department of Physics, University of Otago, Dunedin, New Zealand, ²British Antarctic Survey (NERC), Cambridge, UK,

³Department of Physics and Astronomy, University of Iowa, Iowa City, Iowa, USA, ⁴Space Science and Application Group, Los Alamos National Laboratory, Los Alamos, New Mexico, USA

Abstract Electromagnetic ion cyclotron (EMIC) waves are thought to be important drivers of energetic electron losses from the outer radiation belt through precipitation into the atmosphere. While the theoretical possibility of pitch angle scattering-driven losses from these waves has been recognized for more than four decades, there have been limited experimental precipitation observations to support this concept. We have combined satellite-based observations of the characteristics of EMIC waves, with satellite and ground-based observations of the EMIC-induced electron precipitation. In a detailed case study, supplemented by an additional four examples, we are able to constrain for the first time the location, size, and energy range of EMIC-induced electron precipitation inferred from coincident precipitation data and relate them to the EMIC wave frequency, wave power, and ion band of the wave as measured in situ by the Van Allen Probes. These observations will better constrain modeling into the importance of EMIC wave-particle interactions.

1. Introduction

It has long been recognized that wave-particle interactions with electromagnetic ion cyclotron (EMIC) waves are an important driver for precipitation of relativistic electrons [e.g., *Thorne and Kennel*, 1971; *Summers and Thorne*, 2003; *Thorne*, 2010]. EMIC waves are observed in the Pc1–Pc2 frequency range (0.1–5 Hz). Thermal anisotropy in the ring current proton population (tens to hundreds of keV) causes the waves to be generated near the magnetic equator propagating as left-handed circularly polarized waves [e.g., *Cornwall*, 1965; *Kennel and Petschek*, 1966], hence the term “ion cyclotron.” Recent experimental studies have shown that EMIC wave growth can occur at all local times and can persist for hours and sometimes even days [*Paulson et al.*, 2014; *Saikin et al.*, 2015]. Recent modeling studies have concluded that EMIC waves are very important sources of relativistic and ultrarelativistic electron losses from the outer radiation belt [e.g., *Drozdz et al.*, 2015; *Ni et al.*, 2015].

Despite the decades of recognition that EMIC waves could be significant drivers of electron precipitation, until recently, there has been little experimental evidence of this. However, some progress is now being made. Some of the earliest confirmation comes from ground-based measurements showing evidence of relativistic electron precipitation from subionospheric very low frequency (VLF) and riometer observations along with the start of simultaneous EMIC waves in ground-based magnetometers [*Rodger et al.*, 2008]. Following on from this, the properties of probable EMIC wave precipitation events detected using the expected signature for EMIC wave-driven losses seen in low-Earth orbit satellite data have been presented [*Carson et al.*, 2013]. One of these probable EMIC wave precipitation events was investigated in a case study using multiple ground-based experiments [*Clilverd et al.*, 2015] and was confirmed to be intense and EMIC wave driven, but with unexpectedly low-energy cutoffs <400 keV similar to those suggested by *Hendry et al.* [2014]. At highly relativistic electron energies, indirect evidence of the efficiency of EMIC waves to drive losses has been provided by Canadian ground-based magnetometer data and >2.3 MeV trapped relativistic electron from the Van Allen Probes [*Usanova et al.*, 2014]. Thus, although there is increasing evidence of electron precipitation from EMIC waves, the detailed characteristics of the precipitation and associated waves remain uncertain.

However, there are many examples in the literature where EMIC waves are observed on the ground or in space for which there appears to be no electron precipitation occurring, even when the measurements are available [e.g., *Usanova et al.*, 2014; *Engebretson et al.*, 2015]. There is also a growing recent experimental evidence which suggests that EMIC waves may precipitate electrons with energies as low as a few hundred

keV [Hendry *et al.*, 2014; Clilverd *et al.*, 2015; Blum *et al.*, 2015] rather than the relativistic energies which are widely produced in theoretical modeling [e.g., Meredith *et al.*, 2003; Chen *et al.*, 2011; Usanova *et al.*, 2014]. There is some theoretical support for such comparatively low energy thresholds for EMIC-driven electron precipitation. The minimum resonant energy for a He band EMIC wave inside the plasmasphere was shown to be as low as ~ 100 keV for waves at ~ 1 Hz [Omura and Zhao, 2013, Figure 2], and some quasi-linear theory has indicated minimum resonance energies of ~ 300 – 400 keV [Summers and Thorne, 2003; Ukhorskiy *et al.*, 2010].

In order to better constrain modeling and understand the importance of EMIC wave-particle interactions, it is necessary to have in situ observations of the wave and plasma characteristics for EMIC waves which are confirmed to be driving electron precipitation. In this paper we provide in situ observations supported by ground-based precipitation measurements to fulfill this goal. We provide a detailed description of one event, identifying for the first time the location, size, and energy range of EMIC-induced electron precipitation caused by waves with in situ measurements of EMIC wave frequency, wave power, and ion band. We also provide the wave and plasma parameters for four other similar events.

2. Experimental Data Sets

2.1. Van Allen Probes Observations

We make use of multiple experiments on board the Van Allen Probes, in particular the magnetometer and wideband observations from the Electric and Magnetic Field Instrument Suite and Integrated Science (EMFISIS) [Kletzing *et al.*, 2013], including the cold plasma densities measurements [Kurth *et al.*, 2015]. EMFISIS provides observations of the EMIC waves as well as the geomagnetic field intensities. Pitch angle resolved electron fluxes are provided by the Magnetic Electron Ion Spectrometer (MagEIS) [Blake *et al.*, 2013] and the Relativistic Electron-Proton Telescope (REPT) [Baker *et al.*, 2013] instruments.

2.2. Low-Earth Orbit Precipitation Observations

One source of precipitation observations comes from the Medium Energy Proton and Electron Detector (MEPED) instrument on board the Polar-orbiting Operational Environmental Satellite (POES) [Evans and Greer, 2004]. This data set is unusual in that it measures precipitation electron fluxes inside the bounce loss cone. The characteristics of the POES electron precipitation measurements have been comprehensively described in the literature [e.g., Rodger *et al.*, 2010a, 2010b; Carson *et al.*, 2013].

2.3. Ground-Based Observations

The other source of precipitation observations comes from narrowband subionospheric VLF sites that are part of the Antarctic Arctic Radiation-belt Dynamic Deposition-VLF Atmospheric Research Konsortia (AARDDVARK) network [Clilverd *et al.*, 2009] (for further information see the description of the array at www.physics.otago.ac.nz/space/AARDDVARK_homepage.htm). Subionospheric VLF responds to electron precipitation which penetrates beneath the lower boundary of the ionosphere, that is, electrons with minimum detectable electron precipitation energies of ~ 150 keV (day) and ~ 50 keV (night) [Rodger *et al.*, 2012].

3. EMIC Event on 24 September 2013—Wave Activity

Figure 1 presents a set of spectrograms showing an EMIC event which started at 16:42 UT on 24 September 2013 observed by EMFISIS on board RBSP-A. Figure 1 (first to third panels) shows the three components of the magnetic field in GSM coordinates. Figure 1 (fifth panel) shows the variation in the magnitude of the geomagnetic field, also observed by the EMFISIS magnetometer (Figure 1 (fourth panel) shows the variation in the *SYM-H* geomagnetic index). Shortly before the onset of the EMIC wave the geomagnetic field changes, with the magnitude of the total field altering by ~ 30 nT (i.e., $\sim 14\%$) in 4 min from 16:40 UT. This change can also be seen in the He and O ion gyrofrequencies which are plotted as white lines in the spectrogram panels.

This is a fairly strong and clear example of a He band EMIC wave event. A summary of the wave and plasma properties determined from the EMFISIS observations of this event is given in Table 1. The observations indicate that this event occurred in the afternoon sector and about $0.6 R_E$ inside the plasmapause.

Figure 2 (top) shows a spectrogram of the EMFISIS magnetic field extremely low frequency (ELF) and VLF observations from RBSP-A across the same time period as shown in Figure 1. Here the spectrograms of the summed magnetic field components have been taken. Figure 2 (bottom) shows the wave normal angle for

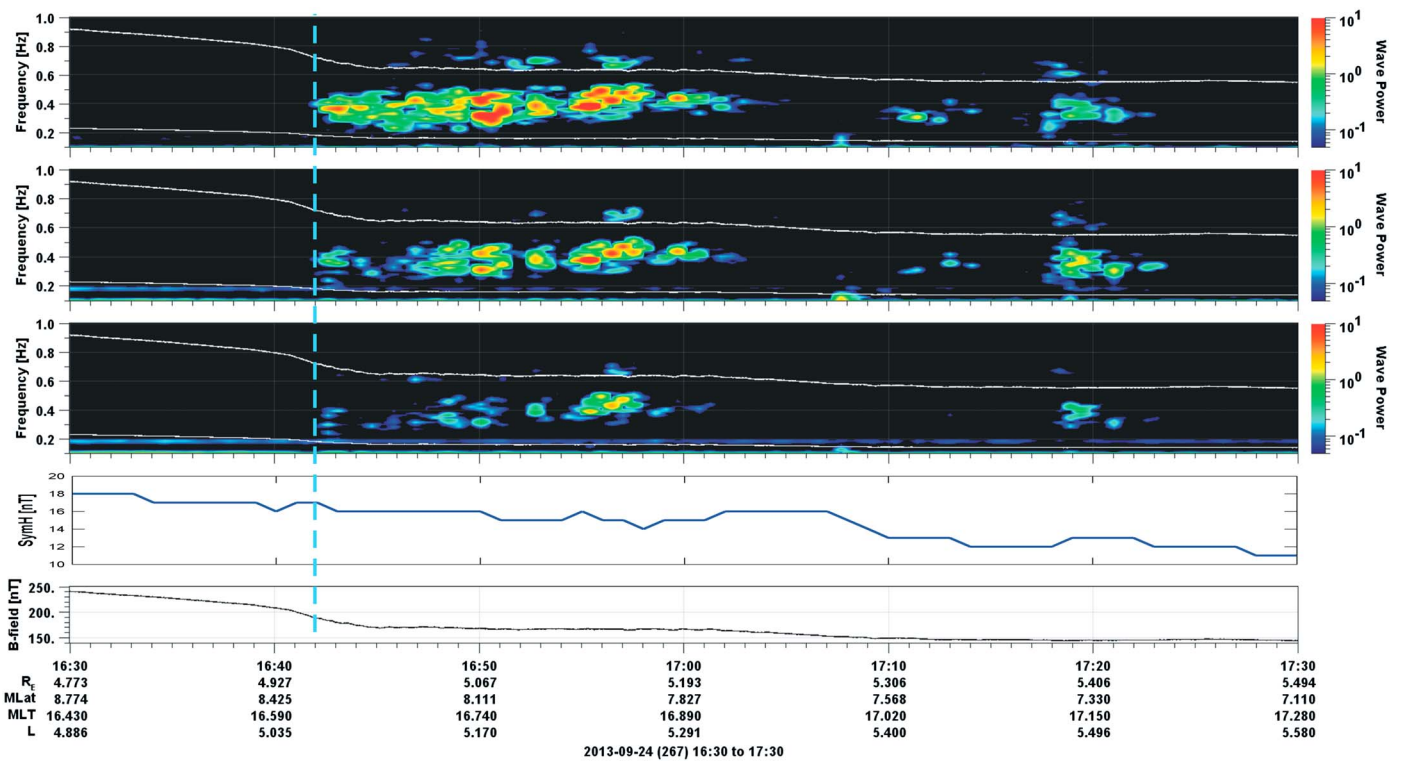


Figure 1. (first to third panels) Spectrograms of the three components of the magnetic field in GSM coordinates from the EMFISIS experiment on board RBSP-A on 24 September 2013. Wave power has units of nT^2/Hz . The white lines show the local ion gyrofrequencies for He (top) and oxygen (bottom) ions. (fourth panel) The SYM-H geomagnetic index. (fifth panel) The absolute value of the DC magnetic field reported by the same instrument. A blue dashed line marks the start of the EMIC wave at 16:42 UT.

the observations shown in Figure 2 (top). Typically, signals with wave normal angles $<45^\circ$ are likely to be whistler mode waves, while those $>75^\circ$ would be indicative of magnetosonic waves [Gurnett and Bhattacharjee, 2005] that are restricted to the region of the geomagnetic equator. Figure 2 indicates that the ELF-VLF wave activity in the time period considered is quiet. Around this time there is an $\sim 100\text{--}200$ Hz magnetosonic wave that is fading out, as well as a weak $\sim 50\text{--}90$ Hz magnetosonic wave which starts around the time of the geomagnetic field decrease. Whistler mode wave activity is weak, particularly in the time period of the strong EMIC wave. It is well known that whistler mode waves can pitch angle scatter electrons

Table 1. Properties at the Times of the Observed EMIC Wave-Driven Precipitation Events^a

	Date (Time: UT)				
	24 Sep 2013 (16:41)	24 Mar 2013 (6:57)	14 Aug 2013 (4:57)	27 Aug 2013 (15:52)	27 Aug 2013 (16:52)
L	5.1	5.7	5.3	5.3	5.8
MLT	16.5	23.7	18.1	17.9	18.7
f_{upper} (Hz)	0.5	0.9	0.4	0.55	0.35
f_{lower} (Hz)	0.25	0.3	0.2	0.47	0.15
PSD wave power					
Typical (nT^2/Hz)	0.8	0.1	3	0.3	0.3
Peak (nT^2/Hz)	10	1	42	2	6
N_e (cm^{-3})	190	79	63	112	43
f_{pe} (kHz)	120	80	72	95	58
f_{ce} (kHz)	5.5	3.9	4.3	4.9	3.1
RBSP satellite	A	B	B	A	A
Ion band	He	H	He	He	He

^aThe first event is that described in detail in this study. The parameters listed are as measured by RBSP. f_{upper} , f_{lower} : upper and lower EMIC wave frequencies, PSD: EMIC wave power spectral density, N_e : cold electron density, f_{pe} : electron plasma frequency, and f_{ce} : electron gyrofrequency.

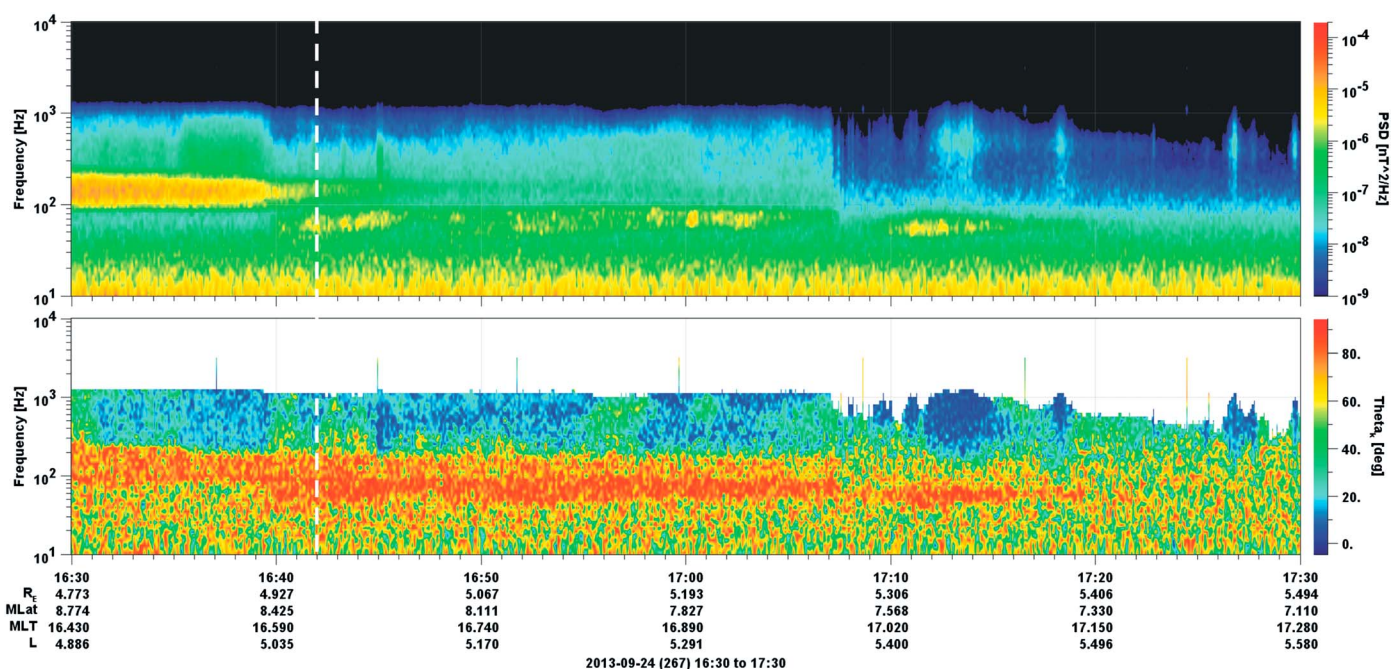


Figure 2. EMFISJIS ELF/VLF magnetic field observations for the same time period shown in Figure 1. (top) Spectrogram of the summed magnetic field components with units of nT^2/Hz . (bottom) Wave normal angle with units of degrees, determined from Figure 2 (top) waveforms.

and cause precipitation [e.g., *Thorne, 2010*], whereas magnetosonic waves are up to 2 orders of magnitude less effective at driving precipitation [*Shprits et al., 2013*].

4. Precipitation Observations

4.1. AARDDVARK

At 16:42 UT the Northern Hemisphere footprint of the RBSP-A spacecraft was located near Iceland. We have examined AARDDVARK data at this time, concentrating on Atlantic longitude observations in the region of the RBSP-A observations. Figure 3 (top row) shows examples of the AARDDVARK observations made from St. John's, Canada (STJ, red line), and Reykjavik, Iceland (REK, blue line). The amplitude and phase perturbations for two transmitters are plotted, with call sign NRK (red line in the figure, located in Iceland) and NDK (blue line, located in North Dakota, USA). Figure 3 presents the change in amplitude and phase relative to undisturbed conditions, i.e., the change relative to the quiet day curve. There are clear amplitude perturbations starting at 16:42 UT (marked by the dashed vertical line). We observe consistent evidence of subionospheric perturbations beginning at the start time of the RBSP-observed EMIC wave seen in Figure 1. As there is no significant whistler mode wave activity occurring at this time (as shown in Figure 2), the EMIC wave is the most likely candidate for driving the electron precipitation causing the observed AARDDVARK precipitation.

Figure 3 (bottom) shows a geographic map of the AARDDVARK paths analyzed in this study. Note that there is both an AARDDVARK receiver and a VLF transmitter in Iceland, with the NRK transmitter symbol largely obscured. In this plot AARDDVARK paths which were seen to respond to precipitation at the EMIC wave start time are shown in green, while the unresponsive paths are shown as dashed light blue lines.

The AARDDVARK observations are clearly consistent with precipitation occurring near Iceland around the L shells of the RBSP footprint. The size of the precipitation patch is sufficiently wide enough that transmitter receiver paths to the immediate east and west of Iceland are affected but not so wide to affect those paths from western European transmitters to Finland or from NPM to the Antarctic station, Halley. The observed region of the EMIC-driven precipitation covers ~ 13 – 17 magnetic local time (MLT).

4.2. POES Observations

Near the start of the period during which the EMIC wave was observed by RBSP-A, there was a serendipitous conjunction with NOAA 15, one of the POES that have been extensively used to investigate radiation belt

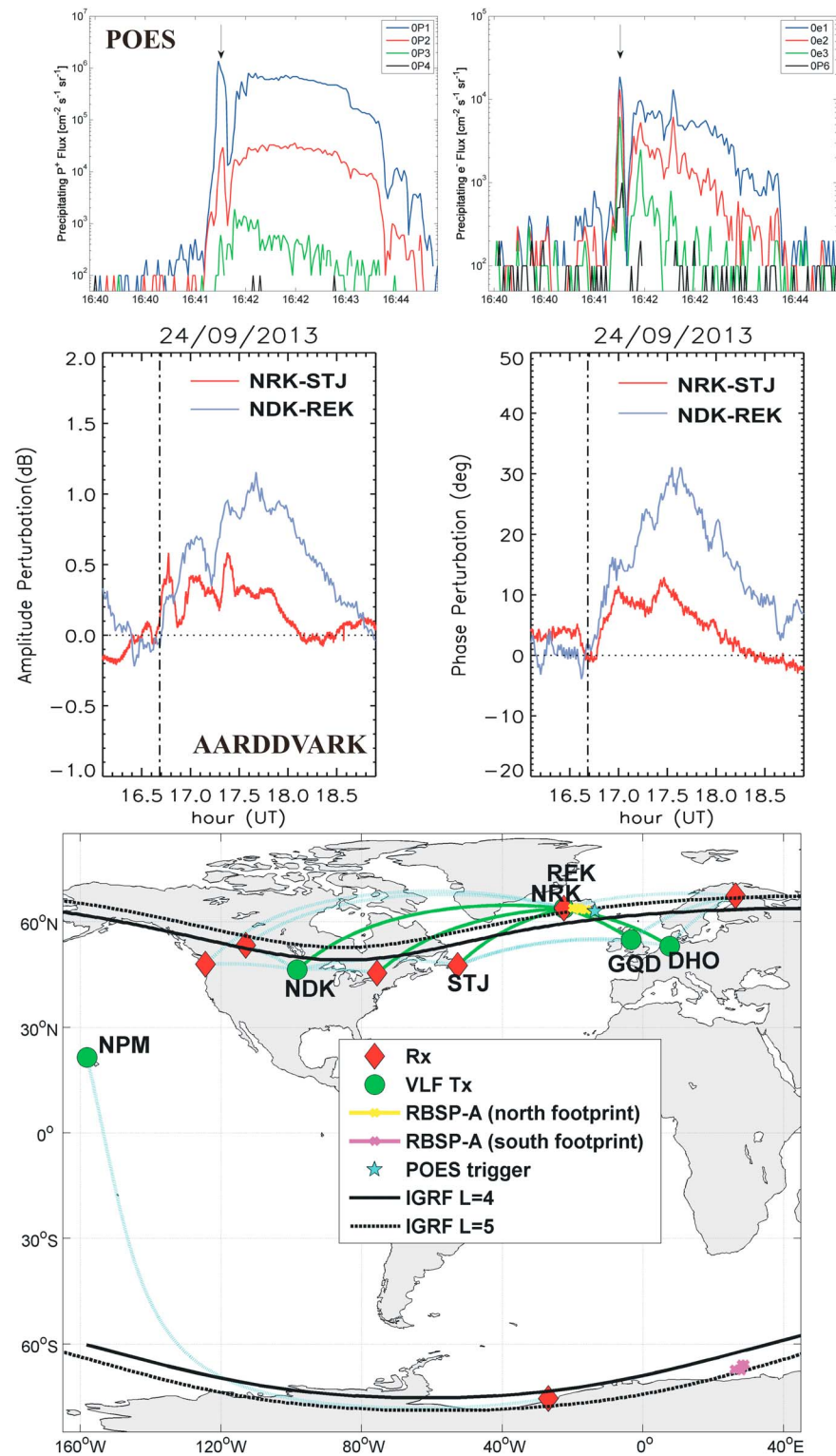


Figure 3. Summary of precipitation observations at the event time. (top row) Precipitating proton (left) and electron (right) fluxes from NOAA 15. (middle row) The AARDDVARK amplitude and phase perturbations observed on the path NRK-St John's (Canada) (STJ, red) and NDK-Reykjavik (REK, blue). The black dashed line marks 16:42 UT. (bottom) Map of the AARDDVARK paths analyzed in this study. RBSP-A northern (yellow) and southern (magenta) footprints are shown, as is the POES trigger subsatellite point (blue star), AARDDVARK receivers (red diamonds), and VLF transmitters (green circles). In this plot AARDDVARK paths which were seen to respond to precipitation at the EMIC wave start time are shown in green, while the unresponsive paths are shown as dashed light blue lines.

precipitation. The orbital track of NOAA 15 passed from south to north at the eastern edge of Iceland. At 16:41:55 UT the MEPED instrument on board this satellite observed a burst of proton and electron precipitation with the signature expected from EMIC waves [Sandanger *et al.*, 2009], detected by an automatic algorithm [Carson *et al.*, 2013]. The NOAA 15 precipitating proton and electron and the automatically detected trigger event (marked by the arrow) are shown in Figure 3 (top row). The location of this algorithm trigger event is shown as the blue star in Figure 3 (bottom), very close to the eastern end of the RBSP-A atmospheric footprint. As this observation was made at essentially the same location and time as the start of the RBSP-A EMIC wave observation, the precipitation includes both protons and a strong relativistic component as expected for effective EMIC wave scattering, and RBSP-A reports no significant ELF/VLF wave activity; we assume that the POES precipitation event was produced by the observed EMIC wave.

The precipitation spike has been analyzed as described in section 3.2 of Clilverd *et al.* [2015]. By using the proton and electron precipitation measurements and a detailed understanding of the instrument response [Yando *et al.*, 2011], one can determine an energy spectrum, flux magnitude, and energy cutoff estimations for the observed precipitation. This precipitation event is best fit with a power law, with spectral gradient values from -2.7 to -1.7 , lower energy precipitation cutoffs of 140–230 keV, upper cutoff estimates of 1.6–8 MeV, and precipitation magnitudes of $\sim 1.25 \times 10^4 \text{ cm}^{-2} \text{ sr}^{-1} \text{ s}^{-1}$.

4.3. AARDDVARK Modeling

The location of the POES triggers event, and the RBSP-A footprints provide useful constraints on the likely longitudinal range of the precipitation affecting the paths from GQD and DHO to Iceland, i.e., the transmitters to the east of the Reykjavik receiver. We undertake modeling of the subionospheric perturbations predicted from precipitation defined by the POES energy and power law gradient, using approaches previously described [e.g., Rodger *et al.*, 2012; Clilverd *et al.*, 2015].

We find that the modeling is sensitive to the initial conditions, for example, comparatively small changes in the starting location of the energetic electron precipitation change along the path (i.e., changes of tens of kilometers). This is likely due to the relatively short, all sea path from the transmitter to receiver, such that there is a high number of significant modes present in the Earth ionosphere waveguide and also the small ionospheric region affected. Our modeling of the perturbations observed on the transmissions from DHO ($\Delta\text{Amplitude} = +1.8 \text{ dB}$, $\Delta\text{Phase} = -3^\circ$) and GQD ($\Delta\text{Amplitude} = +0.6 \text{ dB}$, $\Delta\text{Phase} = -3^\circ$), at the EMIC wave onset time, indicates that these changes are consistent with the effect caused by imposing the POES precipitation observations, i.e., flux magnitudes of $\sim 0.6\text{--}5 \times 10^4 \text{ cm}^{-2} \text{ sr}^{-1} \text{ s}^{-1}$. The modeling reproduces the observations for power law gradients which have low-energy cutoffs, i.e., $\sim 200 \text{ keV}$. It was not possible to successfully model the subionospheric VLF perturbations using low-energy cutoffs of $\sim 1 \text{ MeV}$. Such cutoffs produce much larger amplitude and phase perturbations than observed.

5. Trapped Electron Flux Observations

Figure 4 shows the RBSP-A MagEIS pitch angle resolved trapped fluxes with 1 MeV (top) and 225 keV energies (bottom). At the time of the geomagnetic field change and the start of the EMIC wave the fluxes change to a butterfly distribution, with a 50% decrease in the 90° pitch angle fluxes from 16:41 to 16:44 UT. A similar signature is seen in the MagEIS fluxes at energies $>143 \text{ keV}$ and in REPT fluxes $\leq 2.6 \text{ MeV}$. The REPT fluxes $>2.6 \text{ MeV}$ are at noise levels. There is no evidence of significantly different behavior between the 2.6 MeV fluxes and those at lower energies, in apparent contradiction to the conclusions of Usanova *et al.* [2014], although this could be obscured by the changes leading to the butterfly distribution.

Such butterfly distributions can be produced by magnetopause shadowing or by field line stretching and drift shell splitting [e.g., Roederer, 1970; Sibeck *et al.*, 1987] or by chorus and magnetosonic waves [Xiao *et al.*, 2015]. However, this does not explain the observations in our case, due to the small time dispersion between the energies. The source of the distribution should be only $\sim 0.6 \text{ MLT}$ away to be consistent with the energy dispersion observed (i.e., located at $\sim 16 \text{ MLT}$). While we note that the butterfly distribution is unlikely to be caused by magnetopause shadowing as the location is far from magnetic noon, there has not been evidence suggesting that such pitch angle distributions can be produced by EMIC waves. Nonetheless, the change to this distribution makes it essentially impossible to see evidence of the pitch angle scattering driving the observed precipitation.

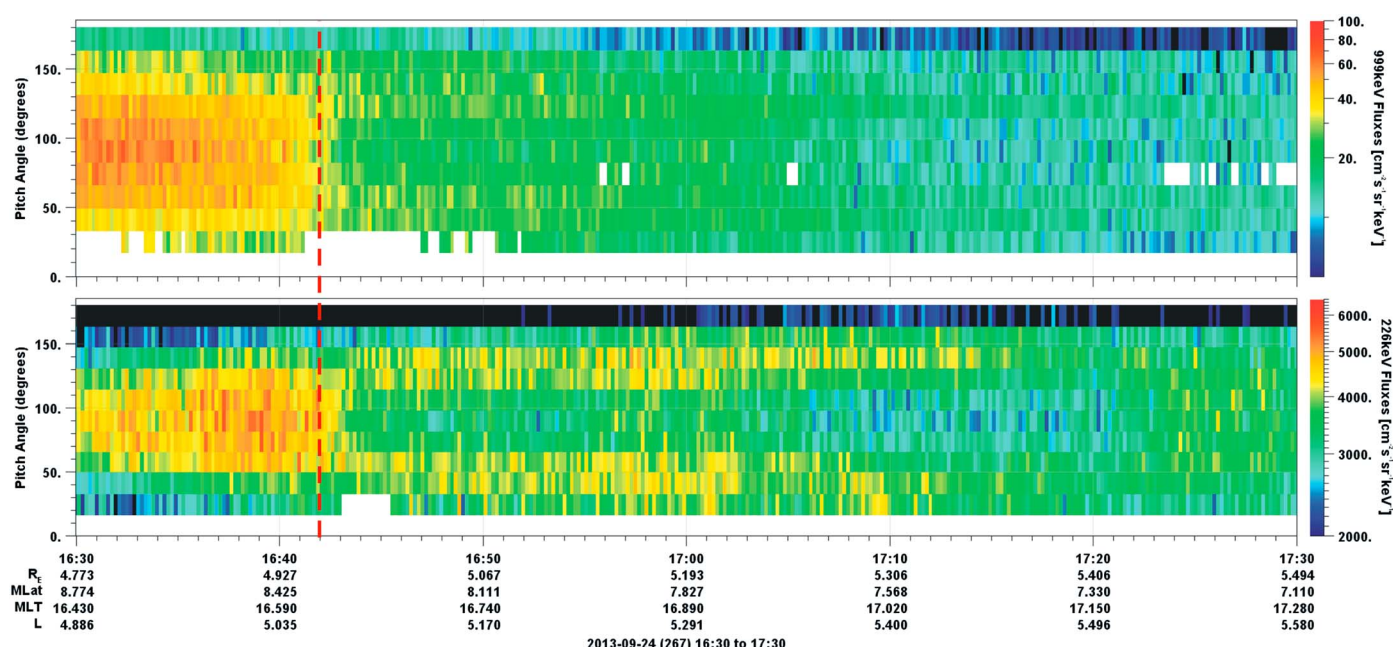


Figure 4. Butterfly pitch angle distributions seen in the MagEIS (top) 1 MeV flux distributions and the (bottom) 225 keV distributions. The dashed red line marks the start of the EMIC wave seen in Figure 1.

6. Additional Events

In our examination of RBSP-A EMIC wave data and comparison with precipitation data we found four other events in which RBSP-A observed an EMIC wave, there was little evidence of confounding ELF/VLF whistler mode wave activity, and AARDDVARK sites at Churchill (Canada), Fairbanks (Alaska), and Sodankylä (Finland) confirmed the presence of energetic electron precipitation. The RBSP-A in situ measurements of EMIC wave and plasma parameters for these four additional events, along with those for 24 September 2013, are given in Table 1. All of these five events have butterfly distributions in the MagEIS trapped electron fluxes which begin near the wave start time. To the best of our knowledge such distributions have not been observed in other published studies describing near-equatorial particle distributions associated with EMIC waves.

In the current study we have chosen to concentrate on the analysis of the 24 September 2013 event, due to the serendipitous conjunctions between RBSP-A, NOAA 15, and AARDDVARK network observations. None of the other events listed in Table 1 have such close conjunctions. We note that there are multiple POES triggers on 27 August 2013 and that the events on this day may deserve more attention in a future study.

7. Summary

For the first time we have combined satellite-based observations of the characteristics of EMIC waves, with satellite and ground-based observations of the EMIC-induced electron precipitation. In a detailed case study, supplemented by an additional four examples, we are able to identify the location of the EMIC-induced electron precipitation inferred from coincident POES/AARDDVARK data and relate them to the EMIC wave frequency, PSD wave power, and ion band as measured by the Van Allen Probes. We have also constrained the size and energy range of the electron precipitation.

We find the following:

1. The precipitation-causing EMIC waves typically occur over the MLT range 16–00 UT and at $L \sim 5.4 \pm 0.4$, somewhat inside the plasmopause. The frequency of the EMIC waves is typically 0.3–0.5 Hz and is mostly found within the helium band. The typical wave power spectral density is $\sim 1 \text{ nT}^2/\text{Hz}$, with peak powers ~ 10 times higher.

2. The EMIC-induced electron precipitation was detected by the ground-based AARDDVARK network, with one coincident measurement made by one of the NOAA POES. The region of electron precipitation was small in geomagnetic latitude, i.e., <50 km ($\Delta L = 0.15$), but high in flux, i.e., $\sim 10^4$ cm $^{-2}$ sr $^{-1}$ s $^{-1}$, with a power law energy spectrum beginning at ~ 200 keV. Radio wave propagation modeling of the AARDDVARK observations is supportive of the POES detection of a narrow latitudinal precipitation patch, as well as extended in longitude through several hours of MLT, and occurring at the time of the EMIC wave observed by RBSP.

Acknowledgments

The authors would like to thank Richard Yeo for hosting the AARDDVARK receiver in Reykjavik and the following institutional AARDDVARK hosts: Churchill Northern Studies Center USGS/Magnetic Observatories Fairbanks and Sodankylä Geophysical Observatory. We would also like to acknowledge the researchers and engineers of NOAA's Space Environment Center for the provision of the data and the operation of the SEM-2 instrument carried on board these spacecraft, the many teams involved in the Van Allen Probes, and the developers of the Autoplot interactive data tool. The research at University of Iowa was supported by JHU/APL contract 921647 under NASA prime contract NASS-01072. Data availability is described at the following websites: <http://rbspgway.jhuapl.edu/> (Van Allen Probes Science Gateway), <http://emfisis.physics.uiowa.edu/> (EMFISIS), http://www.rbsep-ect.lanl.gov/data_pub/rbspa/mageis/level3/ (MagEIS), http://www.rbsep-ect.lanl.gov/data_pub/rbspb/rept/level3/ (REPT), http://www.rbsep-ect.lanl.gov/data_pub/rbspa/MagEphem/def/2013/ (MagEphem), <http://satdat.ngdc.noaa.gov/sem/poes/data/> (POES SEM-2), http://www.physics.otago.ac.nz/space/AARDDVARK_homepage.htm (AARDDVARK), and <http://wdc.kugi.kyoto-u.ac.jp/aeasy/index.html> (SYM-H).

References

- Baker, J. B., et al. (2013), The Relativistic Electron-Proton Telescope (REPT) instrument on board the Radiation Belt Storm Probes (RBSP) spacecraft: Characterization of Earth's radiation belt high-energy particle populations, *Space Sci. Rev.*, **179**, 337–381, doi:10.1007/s11214-012-9950-9.
- Blake, J. B., et al. (2013), The Magnetic Electron Ion Spectrometer (MagEIS) instruments aboard the Radiation Belt Storm Probes (RBSP) spacecraft, *Space Sci. Rev.*, **179**, 383–421, doi:10.1007/s11214-013-9991-8.
- Blum, L. W., et al. (2015), Observations of coincident EMIC wave activity and duskside energetic electron precipitation on 18–19 January 2013, *Geophys. Res. Lett.*, **42**, 5727–5735, doi:10.1002/2015GL065245.
- Carson, B. R., C. J. Rodger, and M. A. Clilverd (2013), POES satellite observations of EMIC-wave driven relativistic electron precipitation during 1998–2010, *J. Geophys. Res. Space Physics*, **118**, 232–243, doi:10.1029/2012JA017998.
- Chen, L., R. M. Thorne, and J. Bortnik (2011), The controlling effect of ion temperature on EMIC wave excitation and scattering, *Geophys. Res. Lett.*, **38**, L16109, doi:10.1029/2011GL048653.
- Clilverd, M. A., et al. (2009), Remote sensing space weather events: The AARDDVARK network, *Space Weather*, **7**, S04001, doi:10.1029/2008SW000412.
- Clilverd, M. A., R. Duthie, R. Hardman, A. T. Hendry, C. J. Rodger, T. Raita, M. Engebretson, M. R. Lessard, D. Danskin, and D. K. Milling (2015), Electron precipitation from EMIC waves: A case study from 31 May 2013, *J. Geophys. Res. Space Physics*, **120**, 3618–3631, doi:10.1002/2015JA021090.
- Cornwall, J. M. (1965), Cyclotron instabilities and electromagnetic emission in the ultra low frequency and very low frequency ranges, *J. Geophys. Res.*, **70**, 61–69, doi:10.1029/JZ070i001p00061.
- Drozhdov, A. Y., Y. Y. Shprits, K. G. Orlova, A. C. Kellerman, D. A. Subbotin, D. N. Baker, H. E. Spence, and G. D. Reeves (2015), Energetic, relativistic, and ultrarelativistic electrons: Comparison of long-term VERB code simulations with Van Allen Probes measurements, *J. Geophys. Res. Space Physics*, **120**, 3574–3587, doi:10.1002/2014JA020637.
- Engelbreton, M. J., et al. (2015), Van Allen probes, NOAA, GOES, and ground observations of an intense EMIC wave event extending over 12 h in magnetic local time, *J. Geophys. Res. Space Physics*, **120**, 5465–5488, doi:10.1002/2015JA021227.
- Evans, D. S., and M. S. Greer (2004), Polar orbiting environmental satellite space environment monitor - 2: Instrument descriptions and archive data documentation, *NOAA Tech. Memo*, version 1.4, Space Environ. Lab., Boulder, Colo.
- Gurnett, D. A., and A. Bhattacharjee (2005), *Introduction to Plasma Physics: With Space and Laboratory Applications*, Cambridge Univ. Press, New York.
- Hendry, A. T., C. J. Rodger, B. R. Carson, and M. A. Clilverd (2014), Investigating the upper and lower energy cutoffs of EMIC-wave driven precipitation events, in *General Assembly and Scientific Symposium (URSI GASS), 2014 XXXIth URSI*, pp. 1–4, IEEE, Beijing, doi:10.1109/URSIGASS.2014.6929964.
- Kennel, C. F., and H. E. Petschek (1966), Limit on stably trapped particle fluxes, *J. Geophys. Res.*, **71**, 1–28, doi:10.1029/JZ071i001p00001.
- Kletzing, C. A., et al. (2013), The electric and magnetic field instrument suite and integrated studies (EMFISIS) on RBSP, *Space Sci. Rev.*, **179**, 127–181.
- Kurth, W. S., S. De Pascuale, J. B. Faden, C. A. Kletzing, G. B. Hospodarsky, S. Thaller, and J. R. Wygant (2015), Electron densities inferred from plasma wave spectra obtained by the Waves instrument on Van Allen Probes, *J. Geophys. Res. Space Physics*, **120**, 904–914, doi:10.1002/2014JA020857.
- Meredith, N. P., R. M. Thorne, R. B. Horne, D. Summers, B. J. Fraser, and R. R. Anderson (2003), Statistical analysis of relativistic electron energies for cyclotron resonance with EMIC waves observed on CRRES, *J. Geophys. Res.*, **108**(A6), 1250, doi:10.1029/2002JA009700.
- Ni, B., et al. (2015), Resonant scattering of outer zone relativistic electrons by multiband EMIC waves and resultant electron loss timescales, *J. Geophys. Res. Space Physics*, **120**, 7357–7373, doi:10.1002/2015JA021466.
- Omura, Y., and Q. Zhao (2013), Relativistic electron microbursts due to nonlinear pitch angle scattering by EMIC triggered emissions, *J. Geophys. Res. Space Physics*, **118**, 5008–5020, doi:10.1002/jgra.50477.
- Paulson, K. W., C. W. Smith, M. R. Lessard, M. J. Engebretson, R. B. Torbert, and C. A. Kletzing (2014), In situ observations of Pc1 pearl pulsations by the Van Allen Probes, *Geophys. Res. Lett.*, **41**, 1823–1829, doi:10.1002/2013GL059187.
- Rodger, C. J., T. Raita, M. A. Clilverd, A. Seppälä, S. Dietrich, N. R. Thomson, and T. Ulich (2008), Observations of relativistic electron precipitation from the radiation belts driven by EMIC waves, *Geophys. Res. Lett.*, **35**, L16106, doi:10.1029/2008GL034804.
- Rodger, C. J., M. A. Clilverd, J. C. Green, and M. M. Lam (2010a), Use of POES SEM-2 observations to examine radiation belt dynamics and energetic electron precipitation into the atmosphere, *J. Geophys. Res.*, **115**, A04202, doi:10.1029/2008JA014023.
- Rodger, C. J., B. R. Carson, S. A. Cummer, R. J. Gamble, M. A. Clilverd, J.-A. Sauvaud, M. Parrot, J. C. Green, and J.-J. Berthelier (2010b), Contrasting the efficiency of radiation belt losses caused by ducted and non-ducted whistler-mode waves from ground-based transmitters, *J. Geophys. Res.*, **115**, A12208, doi:10.1029/2010JA015880.
- Rodger, C. J., M. A. Clilverd, A. J. Kavanagh, C. E. J. Watt, P. T. Verronen, and T. Raita (2012), Contrasting the responses of three different ground-based instruments to energetic electron precipitation, *Radio Sci.*, **47**, RS2021, doi:10.1029/2011RS004971.
- Roederer, J. G. (1970), *Dynamics of Geomagnetically Trapped Radiation*, Springer, New York.
- Saikin, A. A., J.-C. Zhang, R. C. Allen, C. W. Smith, L. M. Kistler, H. E. Spence, R. B. Torbert, C. A. Kletzing, and V. K. Jordanova (2015), The occurrence and wave properties of H $^{+}$, He $^{+}$, and O $^{+}$ -band EMIC waves observed by the Van Allen Probes, *J. Geophys. Res. Space Physics*, **120**, doi:10.1002/2015JA021358.
- Sandanger, M., F. Søråas, M. Sørbo, K. Aarsnes, K. Oksavik, and D. Evans (2009), Relativistic electron losses related to EMIC waves during CIR and CME storms, *J. Atmos. Sol. Terr. Phys.*, **71**(10–11), 1126–1144, doi:10.1016/j.jastp.2008.07.006.
- Shprits, Y. Y., A. Runov, and B. Ni (2013), Gyro-resonant scattering of radiation belt electrons during the solar minimum by fast magnetosonic waves, *J. Geophys. Res. Space Physics*, **118**, 648–652, doi:10.1002/jgra.50108.

- Sibeck, D. G., R. W. McEntire, A. T. Y. Lui, R. E. Lopez, and S. M. Krimigis (1987), Magnetic field drift shell splitting: Cause of unusual dayside particle pitch angle distributions during storms and substorms, *J. Geophys. Res.*, **92**, 13,485–13,497, doi:10.1029/JA092iA12p13485.
- Summers, D., and R. M. Thorne (2003), Relativistic electron pitch-angle scattering by electromagnetic ion cyclotron waves during geomagnetic storms, *J. Geophys. Res.*, **108**(A4), 1143, doi:10.1029/2002JA009489.
- Thorne, R. M. (2010), Radiation belt dynamics: The importance of wave-particle interactions, *Geophys. Res. Lett.*, **37**, L22107, doi:10.1029/2010GL044990.
- Thorne, R. M., and C. F. Kennel (1971), Relativistic electron precipitation during magnetic storm main phase, *J. Geophys. Res.*, **76**, 4446–4453, doi:10.1029/JA076i019p04446.
- Ukhorskiy, A. Y., Y. Y. Shprits, B. J. Anderson, K. Takahashi, and R. M. Thorne (2010), Rapid scattering of radiation belt electrons by storm-time EMIC waves, *Geophys. Res. Lett.*, **37**, L09101, doi:10.1029/2010GL042906.
- Usanova, M. E., et al. (2014), Effect of EMIC waves on relativistic and ultrarelativistic electron populations: Ground-based and Van Allen Probes observations, *Geophys. Res. Lett.*, **41**, 1375–1381, doi:10.1002/2013GL059024.
- Xiao, F., C. Yang, Z. Su, Q. Zhou, Z. He, Y. He, D. N. Baker, H. E. Spence, H. O. Funsten, and J. B. Blake (2015), Wave-driven butterfly distribution of Van Allen belt relativistic electrons, *Nat. Commun.*, doi:10.1038/ncomms9590.
- Yando, K., R. M. Millan, J. C. Green, and D. S. Evans (2011), A Monte Carlo simulation of the NOAA POES Medium Energy Proton and Electron Detector instrument, *J. Geophys. Res.*, **116**, A10231, doi:10.1029/2011JA016671.